Appl. Phys. B (2017) 123:112
DOI 10.1007/s00340-017-6671-5

Applied Physics B
Lasers and Optics

RAPID COMMUNICATION

A compact, transportable single-ion optical clock with 7.8×10^{-17} systematic uncertainty

J. Cao[1,2] · P. Zhang[1,2] · J. Shang[1,2] · K. Cui[1,2] · J. Yuan[1,2] · S. Chao[1,2] · S. Wang[1,2] · H. Shu[1,2] · X. Huang[1,2]

Received: 11 October 2016 / Accepted: 9 February 2017 / Published online: 27 March 2017

Abstract A transportable optical clock based on the $4s^2S_{1/2}$-$3d^2D_{5/2}$ electric quadrupole transition at 729 nm of a single $^{40}Ca^+$ ion trapped in a mini Paul trap has been developed. The physical system of the $^{40}Ca^+$ optical clock is re-engineered from a bulky and complex setup to an integration of two subsystems: a compact single ion unit including ion trapping and detection modules, and a compact laser unit including laser sources, beam distributor and frequency reference modules. The systematic fractional uncertainty has been evaluated to be 7.8×10^{-17}, and the Allan deviation has been rescaled to be $2.3\times10^{-14}/\sqrt{\tau}$ for a single clock by self-comparison with a probe pulse time of 20 ms. Apart from the electronics, the whole setup has been constructed within a volume of 0.54 m^3. This size is to our knowledge currently the best achieved compactness with any type of optical clock. Moreover, this transportable clock is planned to be used for high precision measurements and it's the first step to a space optical clock.

✉ J. Cao
caojian@wipm.ac.cn

X. Huang
hxueren@wipm.ac.cn

[1] State Key Laboratory of Magnetic Resonance and Atomic and Molecular Physics, Wuhan Institute of Physics and Mathematics, Chinese Academy of Sciences, Wuhan 430071, China

[2] Key Laboratory of Atomic Frequency Standards, Wuhan Institute of Physics and Mathematics, Chinese Academy of Sciences, Wuhan 430071, China

1 Introduction

Due to the impressive progress in recent years, optical clocks are deemed for the redefinition of SI second in future as they have surpassed the performance of the current primary frequency standard of Cs clocks in both accuracy and stability [1–4]. At the same time, these ultra-precise optical clocks offer new possibilities for high precision tests of fundamental physics [5–8], geophysics [9, 10], improved timekeeping and satellites navigation [11, 12]. On the other hand, a more accurate and direct mean of optical frequency comparison is required for today's best clocks over quite long distance. However, the uncertainty of satellite links is limited and dedicated equipment should be employed [13, 14], and optical fiber links are also not feasible enough especially for intercontinental comparison [15, 16]. For these reasons, it is quite necessary to develop the applicable optical clocks on ground and even in the space.

It is feasible to develop a transportable optical clock in the first stage. Essential characteristics for a transportable optical clock are compact size, proper mass, usability and reliability. In addition to these performances, it should have the possibility of evaluation all the frequency shifts in every environment where it is placed. Undertaking a necessary step towards optical clocks in space, the "Space Optical Clock" (SOC) program of European Space Agency (ESA) aims at accurate transportable ^{87}Sr and ^{171}Yb optical lattice clock demonstrators with an expected performance of fractional uncertainty below 5×10^{-17} and fractional instability below $1\times10^{-15}/\sqrt{\tau}$ [17]. At present, a transportable ^{87}Sr optical lattice clock (excluding electronics) fitting within a volume of <2 m^3 with an uncertainty of 7×10^{-15} has been developed in LENS of Italy [18]. Other similar prototypes are under development in the members of the SOC consortium [19]. To our knowledge, the ^{87}Sr optical lattice

clock installed in an air-conditional car-trailer reported recently is a transportable clock with the best performance on systematic uncertainty of 7.4×10^{-17} and instability of $1.3\times10^{-15}/\sqrt{\tau}$ [20].

In addition to neutral atoms, a trapped $^{40}Ca^{+}$ single-ion is another promising option in the program of transportable optical clocks. Optical clocks based on single trapped ions have their own advantages on the relatively simple scheme of clock system, especially the simplicity on a small number of semiconductor lasers allowing for developing compact, robust and low-cost applicable clocks. Moreover, excellent performance regarding frequency uncertainty and instability make them attractive and cost-effective [21, 22]. In this article, we report on the realization of a transportable optical clock based on the $4s^2S_{1/2}$-$3d^2D_{5/2}$ electric quadrupole transition at 729 nm of $^{40}Ca^{+}$ single-ion trapped in a miniature Paul trap. Apart from the electronics, the whole equipment has been constructed within a volume of 0.54 m^3. The overall systematic fractional uncertainty has been evaluated to be 7.8×10^{-17}, and the Allan deviation has been rescaled to be $2.3\times10^{-14}/\sqrt{\tau}$ for a single clock by self-comparison with a probe pulse time of 20 ms.

2 The transportable clock setup

The design of the transportable $^{40}Ca^{+}$ single-ion optical clock, which is fully operational in our laboratory, is shown in Fig. 1. The physical system of this apparatus is re-engineered from a bulky and complex setup to an integration of two subsystems: a compact single ion subsystem including ion trapping and detection modules, and a compact laser subsystem including laser sources, beam distributor and frequency stabilization modules. All the connections among each modules are provided by single-mode polarization-maintaining fibers. This modular design ensures better stability and reliability which are essential for long-term operation of transportable clock. Moreover, the development in the field of commercial optoelectronic subcomponents allows for independent testing and maintenance of each modules, such as a simple replacement or promotion of components.

The ion system, shown in Fig. 2a, consists of a compact vacuum chamber with a cuboid trapping region (size: $7\times7\times7$ cm^3) which is kept to below 5×10^{-8} Pa by a 10 L/s ion pump. A miniature ring-endcap ion trap optimized by finite element analysis method for more close to an ideal hyperboloidal trap, with a center-to-ring electrode distance of $r_0 \approx 0.75$ mm and an endcap-to-center distance of $z_0 \approx 0.75$ mm [23]. This trap is driven by a helical resonator at $\Omega_{rf} \approx 2\pi \times 24.54(10)$ MHz at which the rf-induced second-order Doppler frequency shift and Stark shift cancel each other approximately [24, 25]. The background magnetic field is reduced to $B \approx 2.2$ μT by two layers of magnetic shielding. Laser-induced fluorescence emitted by the $^{40}Ca^{+}$ single-ion at 397 nm is collected by a custom-made objective (numerical aperture = 0.32, optical aperture = 35 mm) which is fixed to the vacuum window to ensure the stability of the module during transporting. All the photons collected by the objective are send to a photomultiplier (PMT), and both a narrow bandpass filter and an aperture stop are employed to filter the background stray light. Taking into account the collection of the solid angle, the transmittance of optical elements and the quantum

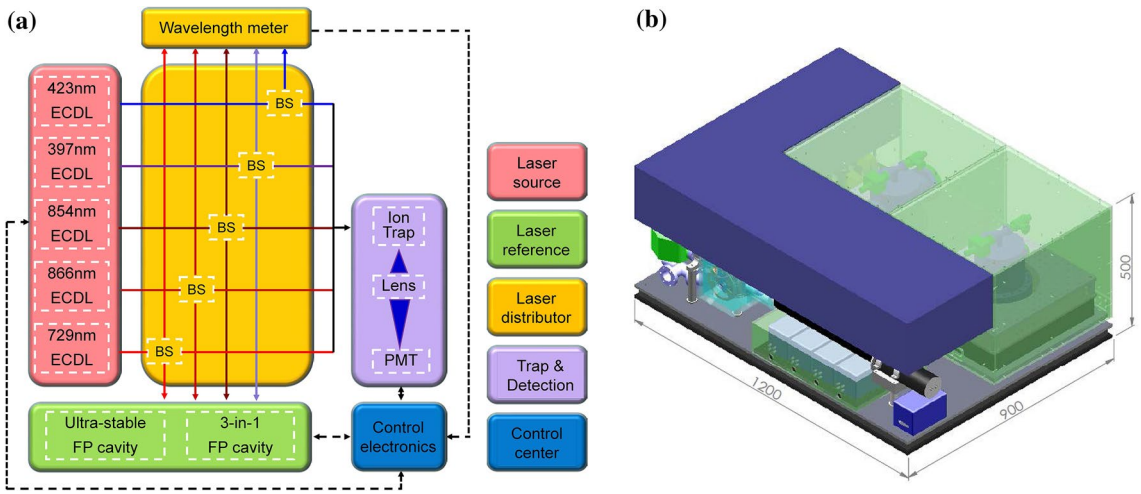

Fig. 1 Design of the transportable single-ion optical clock. **a** Schematic diagram of clock system. **b** Design effect drawing of clock system. The *blue* "L" module is control electronics and the part that is not fully exposed under the electronics is the trap and detection module and laser source module. The rest of the space is mainly occupied by the laser reference modules, which are represented by the *green boxes*

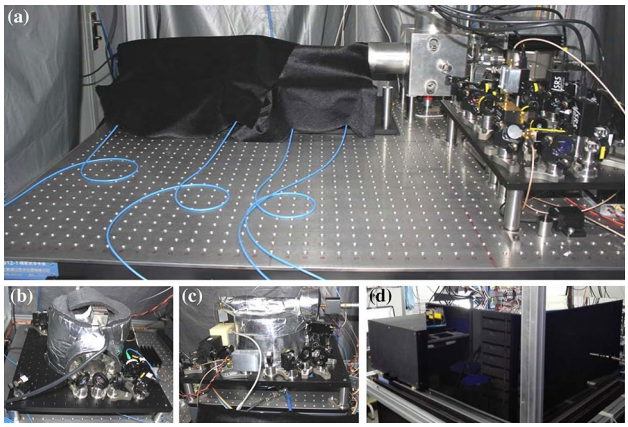

Fig. 2 Overview of the transportable single-ion optical clock. **a** A compact single ion subsystem including ion trapping, detection modules, and laser sources. All of them are placed on a 1.2×0.9 m^2 optical table. The blank place is prepared for **b** the submodule of 3-in-1 cavity for 397/866/854 nm lasers and **c** the submodule of ultra-stable cavity for the 729 nm laser. **d** Integration of the physical system after encapsulation with three *black boxes*. Excluding the electronics, the volume of this transportable clock is about $1.2\times0.9\times0.5$ m^3

efficiency of the PMT, the overall efficiency of this fluorescence detecting module is about 0.002.

The modular design of the compact laser system mainly consists of the following modules: laser sources, laser beam distributor and laser frequency reference. The laser source box contains all of the five external cavity diode lasers (ECDLs) used for operation of $^{40}Ca^+$ single-ion optical clock. The wavelengths of these lasers are 423 nm (photoionization of calcium atoms), 397 nm (Doppler cooling and fluorescence detection), 866 nm (repumping for keeping the cycles of cooling), 729 nm (clock transition probing) and 854 nm (quenching from the metastable state after clock probing). Through the laser beam distributor, consisting of five fiber splitters, each output of these ECDLs is splitted into a few parts and then are coupled to the wavemeter, the ion system and laser frequency reference modules, respectively.

The module of laser frequency reference contains two Fabry–Pérot cavities which are shown in Fig. 2b, c, respectively. One Fabry–Pérot cavity is made from a 10-cm-long 3-in-1 ultra low expansion (ULE) glass used for three lasers (397/866/854 nm, finesse ~100) with three pairs of fused-silica mirrors simultaneously attached for each wavelength [26]. As the cavity is made of ULE glass and sealed in a thermal shield and vacuum chamber which are encapsulated in a box (size: $52\times46\times34$ cm^3), the frequency fluctuation of these lasers is about 1 MHz/day which is acceptable for daily operation. The other Fabry–Pérot cavity is a 10-cm-long all ULE glass cavity including mirrors (finesse ~300,000) used for the 729 nm clock laser. The supporting way of the cavity is simulated for searching for the vibration insensitive points by the method of finite element analysis (FEA) [27, 28], and the setup is placed on a small active vibration isolated platform to reduce the vibration noise. A set of thermal shield and a temperature-controlled vacuum chamber similar to the one used for 3-in-1 cavity are also employed and all of these devices including the compact designed optical components are encapsulated in a box (size: $52\times46\times45$ cm^3) to reduce the influence of thermal fluctuation. After the 729 nm laser is locked to this ultra-stable cavity by the Pound–Drever–Hall (PDH) method, the linewidth is measured to be 1 Hz from a heterodyne beat note with another 729 nm laser system of similar performance and the frequency instability is measured to about 2×10^{-15} at $1\sim100$ s after removing the linear drift which is less than 0.1 Hz/s [29].

3 Clock operation and evaluation of its performance

A single $^{40}Ca^+$ ion is loaded into the trap by effective photoionization of neutral calcium atoms with a 423 nm diode laser beam and a 370 nm LED. Typically, ~10 μW of the 397 nm laser power is focused on the ion with a beam waist of ~50 μm combined with ~350 μW/350 μW/10 nW (beam size ~100 μm) of the 866/854/729 nm laser, respectively. After micromotion minimization with the methods of rf-photo correlation [24] and rf potential modulation [30], the single ion can be trapped for about 1 day continuously with laser Doppler cooling. An on-resonance fluorescence count rate of 40,000/s is obtained for a single ion. For a typical background count rate of 2000/s these results in a signal-to-background ratio of 20. The secular motion frequencies of trapped ion are $\omega_{(r,z)} \approx 2\pi\times(2.1, 4.2)$ MHz when the rf forward power to the helical resonator is 5 W routinely, measured by 'tickling' the ions with low-power rf field applied to the compensation and endcap electrodes, respectively [31].

The 729 nm laser is locked to the TEM_{00} mode of the ultra-stable cavity which is the closest to the clock transition frequency. This frequency difference is covered with a double-passing acousto-optic modulator (AOM) driven by a signal generator referenced to an active hydrogen maser (CH1-75A). This computer-controlled signal generator updates the probe laser frequency every 40 cycles of pulses for spectroscopic measurements and locking to the transition line center by the "four points locking scheme" [32]. The double-passed AOM also serves as a shutter for the probe laser beam. For cancellation of the linear Zeeman shift, the quadrupole shift and the tensor part of the Stark shifts, the laser is locked to the three inner pairs of Zeeman components with magnetic sublevels $m_{j'} = \pm1/2\,, \pm3/2\,, \pm5/2$ in the upper $3d^2D_{5/2}$ state [33],

sequentially in each cycle during the lock runs (Fig. 3a). Each of the six components is measured independently and the resulting line center is combined by averaging the center frequencies of these three pairs of components.

To prevent ac-Stark shifts of the 729 nm clock transition caused by the other 397/866/854 nm lasers, a pulse light sequence is introduced to observe the spectra. In this experiment, the cooling pulse, which includes the 397/866/854 nm radiations, is 15 ms. The 729 nm probe pulse is varied according to the experimental requirements, and it induces a Fourier limited linewidth of 22 Hz with a pulse time of 40 ms (Fig. 3b), while all the other radiations are blocked by mechanical shutters. Buffer time of 3 ms is used before and after the probe pulse to again prevent ac Stark shifts as the actuation time of each shutter is ~2 ms. After the clock probing pulse, the state of the ion is interrogated within 1 ms using 397 nm and 866 nm lasers.

The thermal motion of the ion in the rf trap with secular motion frequency $\omega_{r,z}$ causes Doppler frequency shift. For our ring-endcap trap, the ion temperature is estimated from the intensity of the first-order secular sidebands relative to the carrier [34]. These ratios normally are 0.02 ~ 0.05 for the radial sideband and 0.005 ~ 0.012 for the axial sideband, corresponding to mean temperature of 1.9(0.4) and 4.4(1.8) mK at radial and axial direction, respectively. Taking into account the total kinetic energy of the trapped ion, we get an equivalent temperature of 6.3(1.9) mK, which is nearly one order of magnitude higher than the Doppler cooling limit. However, thanks to the high secular motion frequencies, the single ion is laser-cooled to the Lamb-Dicke regime as the Lamb-Dicke approximation is satisfied well and therefore the first-order Doppler shift is negligible. With the ion temperature estimated, the related second-order Doppler shift is calculated to be −9.0(2.7) mHz [35].

On the other hand, thermal secular motion can push the ion into nonzero mean-square electric fields from the trap, which introduces a Stark shift. This shift can also be calculated from the ion temperature above for the selected three pairs of transition and the average shift is 17.5(5.3) mHz [35].

The excess micromotion can also produce a second-order Doppler shift and a Stark shift. Since it is always one of the greatest contributions of systematic uncertainty for the optical clocks based on an ion in an rf trap, reduction of this micromotion to extremely low level is particularly important. Using an electron multiplying charge coupled device (EMCCD) based imaging system with a resolution limit of ~2 μm (pixel size: 8 μm × 8 μm, magnification of the imaging lens: 5), the possible changes of ion position by any residual trap asymmetry and stray fields can be detected by an EMCCD when alternate the trap confinement between weak and tight (rf power: 2 ~ 5 W) [24]. Then one takes adjustments of the DC voltages on two compensation electrodes in the radial plane and on one of the endcap electrodes until it is unable to distinguish the changes of ion position. This method rapidly converges the system to a low state of micromotion which is parallel to the EMCCD sensor and thus the upper limit can be estimated [22]. Ion displacement perpendicular to the EMCCD sensor will cause micromotion on the *k*-vector direction of the 729 nm laser beam, which can be estimated by measuring the ratio of the micromotion sideband relative to the carrier intensity. This ratio normally is 0.001 ~ 0.008 and the related second-order Doppler shift is calculated to be $\Delta\nu_{\mu,D2} = -18(18)$ mHz [24]. However, considering the Stark shift due to the excess micromotion, the combined shifts can be described by

$$\Delta\nu_{\mu} = \Delta\nu_{\mu,D2}[1 + \Delta\alpha_0 (mc\Omega_{rf})^2/\hbar\omega_0 e^2\ ], \quad (1)$$

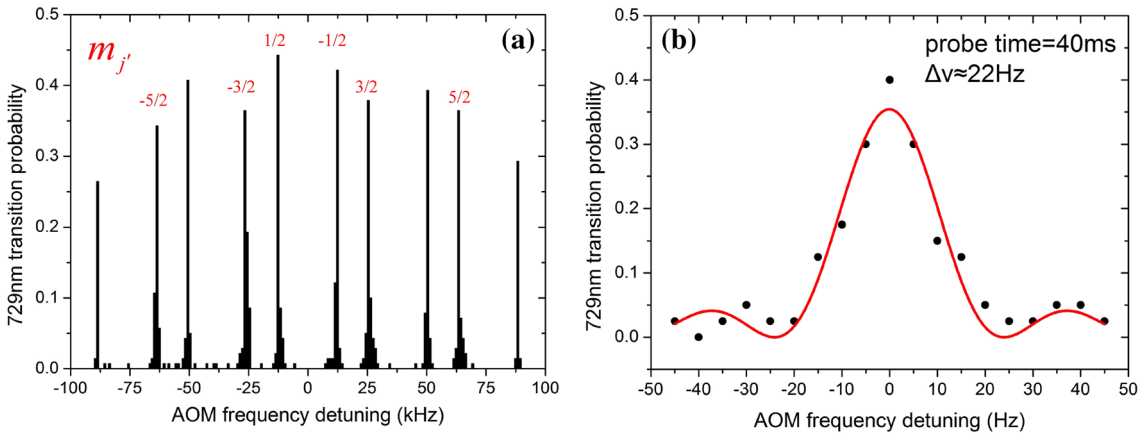

Fig. 3 Zeeman spectra of the $4s^2S_{1/2}$-$3d^2D_{5/2}$ clock transition. **a** Ten components of the Zeeman profile with the whole separation of ~180 kHz in the magnetic field of ~2.2 μT. The six values of $m_{j'}$ of magnetic sublevels in the upper $3d^2D_{5/2}$ state selected for clock operation are shown in *red marks*. **b** Rabi excitation spectrum of the $m_{j'} = 1/2$ component with 729 nm pulse time 40 ms shows the spectral resolution of 22 Hz

where $\Delta\alpha_0$ is the differential static scalar polarizability of clock transition, m the mass of ion, ω_0 the clock transition angular frequency, c the speed of light, $\hbar$ the Plank's constant, and e the charge of an electron. For ions with a negative value of $\Delta\alpha_0$, such as $^{40}Ca^+$, the term in square brackets vanishes when the rf frequency takes the value of $\Omega_0 = e\sqrt{-\hbar\omega_0/\Delta\alpha_0}/mc$. For our trap, which currently works at $\Omega_{rf} \approx 2\pi \times 24.54(10)$ MHz, the term in the square brackets is 0.018(16) and therefore the micromotion shifts are suppressed by a factor of 63 [33]. When applied to the value of the second-order Doppler shift, the combined shifts are cancelled down to the level of $\pm 0.29(29)$ mHz. The estimated total micromotion shifts is thus $-0.33(58)$ mHz and the tiny residual shift is produced by the little lower trap frequency.

The electric quadrupole shift caused by the interaction between the quadrupole moment of the ion and electric field gradient is always a great source of systematic shift. This shift of a magnetic sublevel $m_{j'}$ is given by [36]

$$\Delta f_{EQ} = \nu_{EQ}\left(3\cos^2\theta - 1\right)\left(m_{j'}^2 - j'\left(j'+1\right)/3\right)/4\,, \tag{2}$$

where ν_{EQ} is a characteristic frequency proportional to the electric quadrupole moment and the electric field gradient, and θ is the angle between the applied magnetic field and the electric field gradient. For the selected three pairs of Zeeman components with $m_{j'} = \pm 1/2\,, \pm 3/2\,, \pm 5/2$, there is

$$\sum_{m_{j'}=-j'}^{j'}\left(m_{j'}^2 - j'\left(j'+1\right)/3\right) = 0. \tag{3}$$

It means the net electric quadrupole shift can be cancelled to an extremely high level naturally. Measurements of the selected three pairs of Zeeman components in Fig. 4a provide a diagnostic of the lock performance as the three shifts of Δf_{EQ} must follow a linear dependence on $m_{j'}^2$. For the longest data sets (~30,000 s) with 729 nm probe time of 40 ms, the histogram of measurements of electric quadrupole shift magnitude $A_{EQ} = \nu_{EQ}\left(3\cos^2\theta - 1\right)/4$ is shown in Fig. 4b. It is also in reasonable agreement with Gaussian distribution. The uncertainty of A_{EQ} is employed to evaluate the electric quadrupole shift by a worst-case scenario and thus the total frequency shift is estimated to be 0(31) mHz [33].

The largest frequency shift in our transportable clock is the ac Stark shift induced by the blackbody radiation (BBR) emitted by the ion's environment. Both the temperature difference of the ion trap relative to the vacuum chamber and the temperature fluctuation of the vacuum chamber are evaluated for our system. The complication in this evaluation is that the strong rf trap field will heat the dielectrics which are necessarily implemented into the structure of our ion trap to electrically insulate various conductive components. The FEA is used to calculate the temperature rise of the ion trap parts and the resulting steady-state temperature distribution [37, 38]. The FEA simulation model is validated by comparing the modelling results with temperature measurements on a dummy ion trap in vacuum chamber, which is almost identical to the system used for the transportable clock. The effective temperature rise at the position of the ion is extracted from the FEA simulation results when the simulation results of the temperature rise of the ion trap electrodes agree with the measurement within 0.1%. As indicated in Fig. 5, the temperature rise of the hottest part of the trap setup is 13.19 K under typical clock operation conditions ($\Omega_{rf} \approx 2\pi \times 24.54(10)$ MHz,

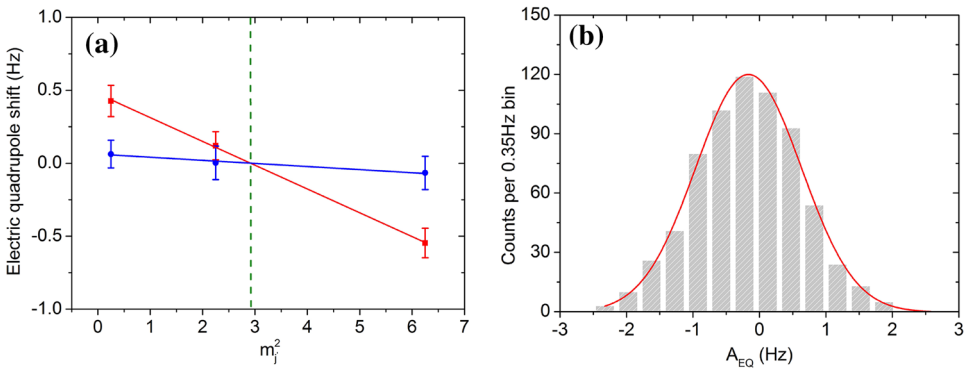

Fig. 4 Measurement of the electric quadrupole shift. **a** Measurement of three pairs of components provides a diagnostic of the lock performance as the three center frequencies must follow a linear dependence on $m_{j'}^2$. Note that only the relative frequency shifts are presented in this figure. For $^{40}Ca^+$, the electric quadrupole shift is cancelled at the intercept of $\Delta m_{j'}^2 = 35/12$, which is shown as the *green dashed line*. The *red* and *blue dots* are corresponding to the measurements at different electric field gradient by an intentional minor change of the voltages applied to trap electrodes. **b** A histogram of the measurements of $A_{\mathrm{EQ}} = \nu_{\mathrm{EQ}}\left(3\cos^2\theta - 1\right)/4$. A_{EQ} is determined experimentally using the frequency difference between shifted pairs: $A_{\mathrm{EQ}} = [\Delta f_{\mathrm{EQ}}(m_{j'} = 5/2\,) - \Delta f_{\mathrm{EQ}}(m_{j'} = 1/2\,)]/6$

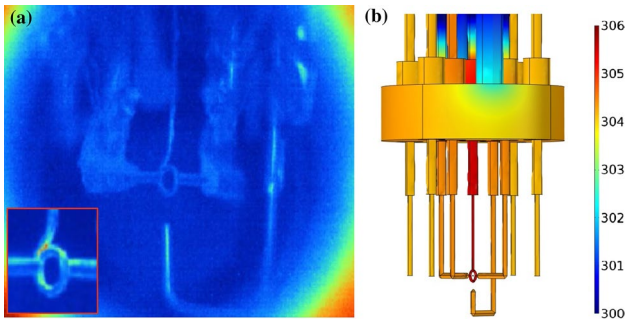

Fig. 5 Evaluation of the temperature distribution of the trap. **a** Enlarged infrared camera images of the dummy trap structure. The large photograph is taken when the rf power is off, and the *inset* is a more enlarged image of the ring and endcap electrodes when rf power is on. The temperature rise due to the rf heating is corrected with a calibrated PT1000. **b** FEM simulation of the temperature distribution of the operational trap for an applied rf potential of 700 V amplitude at 24.54 MHz. A maximum temperature rise of 13.19 K is found on the ring electrode

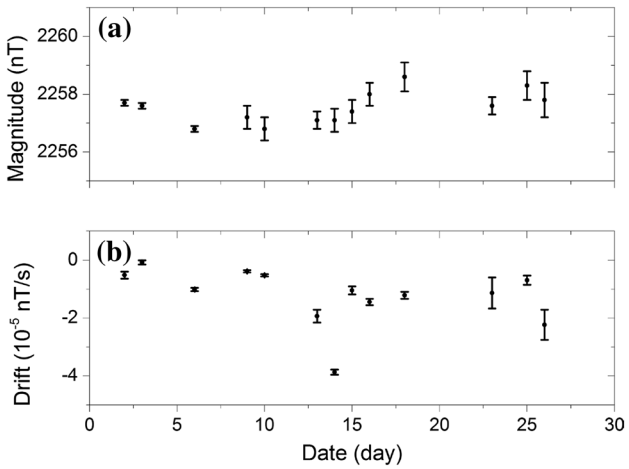

Fig. 6 Measurements of the bias magnetic field and its drift. **a** The magnitudes of bias magnetic field are acquired from statistics of the Zeeman split in different day's clock running. The results between 2256.8 and 2258.6 nT, with a fluctuation less than 0.1%, show a good long-time stability. The bias magnetic field changes slowly from day to day as a combination of room-environmental fluctuation and remanence fluctuation of atom oven. The latter has more effect as the oven is made of stainless steel. In every day's ion loading, the oven is heated in a few minutes and it induces a remanence increase weakly. And then the remanence returns to an original level gradually in a few hours. **b** The slow drifts of bias magnetic field after the heating of oven is finished are also acquired from the evolution of the Zeeman splitting. The magnitude of drift is always less than 4×10^{-5} nT/s

$V_{0P} \approx 700(50)$ V), and the effective temperature rise at the position of ion is 1.72 K, with an uncertainty of 0.44 K mostly attributed to the uncertainty of trap electrodes emissivity. An additional uncertainty of the effective temperature rise at the position of ion of 0.12 K comes from the temperature fluctuation of the vacuum chamber and electrodes of feedthrough. Thus, the effective temperature at the position of ion is 293.92(0.46) K [39], and it results in a BBR frequency shift of 351.2(5.3) mHz [40]. The BBR temperature associated contribution of uncertainty (2.2 mHz) is about a half of the contribution from the differential scalar polarizability (4.8 mHz) [41]. If this polarizability can be measured precisely as similar as $^{88}Sr^{+}$ [42], the total uncertainty of BBR shift could reach the level of 10^{-18} for the $^{40}Ca^{+}$ optical clock in the near future.

The linear Zeeman shift is effectively cancelled out in our experiment by probing on symmetric components. However, the drift of the magnetic field can produce a residual linear Zeeman shift of 29.9 Hz/nT as there is a time interval of 2.0 ~ 2.8 s (729 nm probe time: 20 ~ 40 ms) between each probe point in the clock running. Figure 6 shows the measurements of the bias magnetic field and its drift by statistics of the Zeeman splitting in December 2015. As indicated in Fig. 6b, the magnitude of drift is always less than 4×10^{-5} nT/s and thus the residual linear Zeeman shift is estimated to be 0.0(3.4) mHz by a worst-case scenario. Unlike the first-order Zeeman shift, the quadratic Zeeman effect causes a net shift in the average frequency of a symmetric pair and it can be calculated using second-order perturbation theory. For the bias magnetic field of 2257.7(1.0) nT shown in Fig. 6a, the net frequency shift is calculated to be 73.49(8) μHz. Similarly, the magnetic field associated with BBR can also produce a quadratic Zeeman shift. The BBR field for the effective temperature of 293.92(0.46) K obtained above gives $B_{rms} = 2718.7(4.3)$ nT and the related quadratic Zeeman shift of 106.57(34) μHz [33].

Electromagnetic fields of the lasers incident on the ion during the interrogations can cause an ac Stark shift of the clock transition. For the 397 nm laser, two mechanical shutters are employed to switch off the laser beam. With the first shutter closed during the interrogations, the frequency difference between the status of the second shutter on and off is measured to be 1.67(16) Hz. With an attenuation of >50 dB for the second shutter which switches off the 397 nm laser during the interrogations, the frequency shift is estimated to be 0.017(2) mHz by a worst-case scenario. The frequency shift of the 854 nm laser is estimated with the same method as to the 397 nm laser to be −0.012(3) mHz. Only one shutter is used for the 866 nm laser and the frequency difference between the status of this shutter on and off is measured to be −29.89(33) Hz, and the upper limit of frequency shift is estimated to be −0.299(3) mHz with an attenuation of >50 dB when the shutter is closed. The ac Stark shift produced by the 729 nm laser is calculated by $\Delta\nu_{ac} = \kappa I$, where κ is the coefficient of frequency shift as a function of laser intensity [35]. The average of parameter κ for the selected three pairs of Zeeman components is 0.8(2) mHz/(W/m^2). In our

current clock operation, the laser power incident on the ion is 7(3) nW focused to a spot waist of 137(20) μm, and the related frequency shift is calculated to be 0.19(10) mHz.

The frequency shift resulting from collisions with non-polar gas molecules is estimated using a model based on phase changing Langevin collisions. All the gas is assumed to be composed of H_2 as there is no quadrupole mass analyzer installed with the vacuum chamber. The collisional frequency shift is calculated to be 1.7(1.7) mHz with a measured pressure of $3.0(3.0)\times10^{-8}$ Pa by a worst-case scenario [35].

Table 1 summarizes frequency shifts and the related uncertainties of our transportable $^{40}Ca^{+}$ single-ion clock. The total shift is 361(32) mHz, which corresponds to 7.8×10^{-17} of a fractional uncertainty. This evaluated uncertainty is mainly limited by the statistics of the determination of the electric quadrupole shift which can be reduced by more than one order of magnitude [22] by improving the resolution of clock transition components in the future to achieve the design goal of $\sim1\times10^{-17}$.

The self-comparison method is used to measure the clock stability since only one setup of transportable clock is available currently [43]. As this transportable clock is currently set up in the ground floor of a building which is close to a major street and the violent noises from the environment could broaden and jitter the center frequency of the clock laser at several Hertz level occasionally. So a short 729 nm pulse time of 20 ms with a Fourier limited linewidth more than 40 Hz and a little high value of clock servo gain are used at present for reliable long-time clock running. As a consequence, the stability at situation of a large step of frequency-correction is used, a known cause for stability degradation, is about an order of magnitude worse than the short-term stability of clock laser. Figure 7 shows the Allan deviation as a function of averaging time for the longest data sets lasting more than two days. The rescaled long-term stability of $2.3\times10^{-14}/\sqrt{\tau}$ of the single clock is in reasonable agreement with the calculated quantum projection noise (QPN) limit of $1.9\times10^{-14}/\sqrt{\tau}$ with probe pulse time of 20 ms and dead time of 25 ms [44]. As expected, this rescaled stability is a little higher than the theoretical limit because of laser frequency noise via the Dick effect [43, 45]. Moreover, as the measurements in self-comparison are asynchronous, they cannot benefit from laser noise reduction obtained in a synchronous frequency comparison with two independent clocks [46, 47].

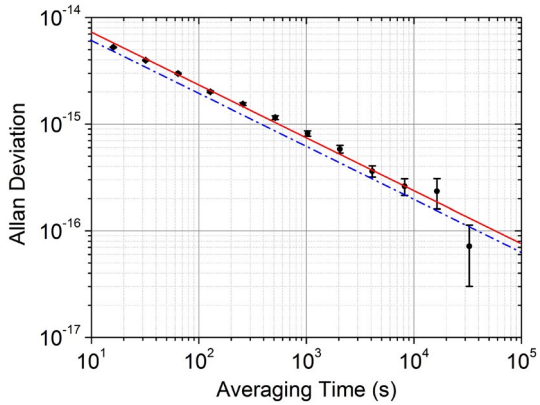

Fig. 7 Allan deviation of the transportable clock as a function of averaging time. The data shown as *dots* is obtained using self-comparison measurements with a probe pulse time of 20 ms and *red solid line* represents a stability of $2.3\times10^{-14}/\sqrt{\tau}$ for a single clock. The QPN limit of $1.9\times10^{-14}/\sqrt{\tau}$ with probe pulse time of 20 ms and dead time of 25 ms is shown by the *blue dash-dot line*

Table 1 Systematic shifts and uncertainties of the transportable clock

Source	Frequency shift		Frequency uncertainty	
	mHz	Fractional	mHz	Fractional
Second-order Doppler shift due to thermal motion	−9.0	−2.19E−17	2.7	6.6E−18
Stark shift due to thermal motion	17.5	4.3E−17	5.3	1.3E−17
Total excess micromotion shifts	−0.33	−8E−19	0.58	1.4E−18
Electric quadrupole shift	0.0	0E−17	31	7.5E−17
Stark shift due to blackbody radiation	351.2	8.54E−16	5.3	1.3E−17
Linear Zeeman shift due to bias field	0.0	0E−18	3.4	8.3E−18
Second-order Zeeman shift due to bias field	0.07349	1.7879E−19	0.00008	1.9E−22
Second-order Zeeman shift due to blackbody radiation	0.10657	2.5927E−19	0.00034	8.3E−22
Stark shift due to 397 nm laser	0.017	4.14E−20	0.002	4.9E−21
Stark shift due to 854 nm laser	−0.012	−2.92E−20	0.003	7.3E−21
Stark shift due to 866 nm laser	−0.299	−7.274E−19	0.003	7.3E−21
Stark shift due to 729 nm laser	0.19	4.6E−19	0.10	2.4E−19
Collisional shift	1.7	4.1E−18	1.7	4.1E−18
Total shifts	361	8.78E−16	32	7.8E−17

4 Conclusion

In summary, we have presented a transportable optical clock based on the $4s^2S_{1/2}$-$3d^2D_{5/2}$ electric quadrupole transition at 729 nm of $^{40}Ca^+$ single ion. The whole equipment of this transportable clock, consisting of a compact single ion subsystem and a compact laser subsystem, is constructed within a volume of 0.54 m^3 excluding the electronics. This is to our knowledge the most compact optical clock of any type. The modular design of this transportable optical clock, allowing for independent test and maintenance, ensures better stability and reliability essential for long-term operation of clock when it moves to another location. The systematic fractional uncertainty has been evaluated to be 7.8×10^{-17}, and the stability is rescaled to be $2.3\times10^{-14}/\sqrt{\tau}$ for a single clock by self-comparison with a probe pulse time of 20 ms. This performance, exceeding the state-of-the-art Cs primary standard by which the SI second is currently realized, makes it a strong candidate for improving worldwide international atomic time (TAI) and widely use as a potential probe for fundamental physics and geophysics. There is a great potential for improving the performance of our transportable clock. The current stability of this transportable optical clock is limited by the coherence time of the clock laser through the maximum probe time which could be improved by a better immunity of the clock laser system to environmental disturbances in the future. The frequency measurement of the transition of the $^{40}Ca^+$ ion in this transportable clock referenced to the SI second is planned as well as the comparisons of the clock transition frequency to other optical clocks.

Acknowledgements We acknowledge Y. Huang, H. Guan and K. Gao for their fruitful discussions and helps. We thank B. Jian for helpful comments on the manuscript. This work is supported by the Ministry of Science and Technology of the People's Republic of China (863 Program, Grant No. 2012AA120701) and the National Natural Science Foundation of China (Grant No. 11674357).

References

1. N. Huntemann, C. Sanner, B. Lipphardt, C. Tamm, E. Peik, Phys. Rev. Lett. **116**(6), 063001 (2016)
2. C.W. Chou, D.B. Hume, J.C.J. Koelemeij, D.J. Wineland, T. Rosenband, Phys. Rev. Lett. **104**(7), 070802 (2010)
3. T.L. Nicholson, S.L. Campbell, R.B. Hutson, G.E. Marti, B.J. Bloom, R.L. McNally, W. Zhang, M.D. Barrett, M.S. Safronova, G.F. Strouse, W.L. Tew, J. Ye, Nat. Commun. **6**, 6896 (2015).
4. I. Ushijima, M. Takamoto, M. Das, T. Ohkubo, H. Katori, Nat Photonics **9**(3), 185–189 (2015).
5. R.M. Godun, P.B.R. Nisbet-Jones, J.M. Jones, S.A. King, L.A.M. Johnson, H.S. Margolis, K. Szymaniec, S.N. Lea, K. Bongs, P. Gill, Phys. Rev. Lett. **113**(21), 210801 (2014)
6. N. Huntemann, B. Lipphardt, C. Tamm, V. Gerginov, S. Weyers, E. Peik, Phys. Rev. Lett. **113**(21), 210802 (2014)
7. S.M. Joao, C. Martins, I. Mota, P.M.T. Vianez, Phys. Lett. B **749**, 389–392 (2015)
8. A. Vutha, New J. Phys **17**, 6 (2015)
9. C.W. Chou, D.B. Hume, T. Rosenband, D.J. Wineland, Science **329**(5999), 1630–1633 (2010)
10. R. Bondarescu, A. Scharer, A. Lundgren, G. Hetenyi, N. Houlie, P. Jetzer, M. Bondarescu, Geophys. J. Int **202**(3), 1770–1774 (2015)
11. T.M. Fortier, M.S. Kirchner, F. Quinlan, J. Taylor, J.C. Bergquist, T. Rosenband, N. Lemke, A. Ludlow, Y. Jiang, C.W. Oates, S.A. Diddams, Nat. Photonics **5** (7), 425–429 (2011).
12. G. Petit, F. Arias, G. Panfilo, C. R. Phys. **16** (5), 480–488 (2015).
13. H. Hachisu, M. Fujieda, S. Nagano, T. Gotoh, A. Nogami, T. Ido, S. Falke, N. Huntemann, C. Grebing, B. Lipphardt, C. Lisdat, D. Piester, Opt. Lett. **39**(14), 4072–4075 (2014)
14. M. Fujieda, D. Piester, T. Gotoh, J. Becker, M. Aida, A. Bauch, Metrologia **51** (3), 253–262 (2014).
15. C. Lisdat, G. Grosche, N. Quintin, C. Shi, S.M.F. Raupach, C. Grebing, D. Nicolodi, F. Stefani, A. Al-Masoudi, S. Dorscher, S. Hafner, J.L. Robyr, N. Chiodo, S. Bilicki, E. Bookjans, A. Koczwara, S. Koke, A. Kuhl, F. Wiotte, F. Meynadier, E. Camisard, M. Abgrall, M. Lours, T. Legero, H. Schnatz, U. Sterr, H. Denker, C. Chardonnet, Y. Le Coq, G. Santarelli, A. Amy-Klein, R. Le Targat, J. Lodewyck, O. Lopez, P.E. Pottie, Nat. Commun. **7**, 7 (2016).
16. T. Takano, M. Takamoto, I. Ushijima, N. Ohmae, T. Akatsuka, A. Yamaguchi, Y. Kuroishi, H. Munekane, B. Miyahara, H. Katori, Nat. Photonics **10** (10), 662–666 (2016).
17. S. Schiller, A. Gorlitz, A. Nevsky, S. Alighanbari, S. Vasilyev, C. Abou-Jaoudeh, G. Mura, T. Franzen, U. Sterr, S. Falke, C. Lisdat, E. Rasel, A. Kulosa, S. Bize, J. Lodewyck, G.M. Tino, N. Poli, M. Schioppo, K. Bongs, Y. Singh, P. Gill, G. Barwood, Y. Ovchinnikov, J. Stuhler, W. Kaenders, C. Braxmaier, R. Holzwarth, A. Donati, S. Lecomte, D. Calonico, F. Levi, 2012 European frequency and time forum (EFTF), 412–418 (2012).
18. N. Poli, M. Schioppo, S. Vogt, S. Falke, U. Sterr, C. Lisdat, G.M. Tino, Appl. Phys. B **117**(4), 1107–1116 (2014)
19. K. Bongs, Y. Singh, L. Smith, W. He, O. Kock, D. Swierad, J. Hughes, S. Schiller, S. Alighanbari, S. Origlia, S. Vogt, O. Sterr, C. Lisdat, R. Le Targat, J. Lodewyck, D. Holleville, B. Venon, S. Bize, G.P. Barwood, P. Gill, I.R. Hill, Y.B. Ovchinnikov, N. Poli, G.M. Tino, J. Stuhler, W. Kaenders, S. O. C. Team, C. R. Phys. **16** (5), 553–564 (2015).
20. S.B. Koller, J. Grotti, S. Vogt, A. Al-Masoudi, S. Dorscher, S. Hafner, U. Sterr, C. Lisdat, arXiv:1609.06183.
21. C. Champenois, M. Houssin, C. Lisowski, A. Knoop, G. Hagel, A. Vedel, F. Vedel, Phys. Lett. A **331**(5), 298–311 (2004)
22. Y. Huang, H. Guan, P. Liu, W. Bian, L. Ma, K. Liang, T. Li, K. Gao, Phys. Rev. Lett. **116**(1), 013001 (2016)
23. J. Cao, X. Tong, K. Cui, J. Shang, H. Shu, X. Huang, Chin. Phys. Lett **31**(04), 43701 (2014)
24. D.J. Berkeland, J.D. Miller, J.C. Bergquist, W.M. Itano, D.J. Wineland, J. Appl. Phys **83**(10), 5025–5033 (1998)
25. A.A. Madej, P. Dubé, Z. Zhou, J.E. Bernard, M. Gertsvolf, Phys. Rev. Lett. **109**(20), 203002 (2012)
26. A. Nevsky, S. Alighanbari, Q.F. Chen, I. Ernsting, S. Vasilyev, S. Schiller, G. Barwood, P. Gill, N. Poli, G.M. Tino, Opt. Lett. **38**(22), 4903–4906 (2013)
27. S.A. Webster, M. Oxborrow, P. Gill, Phys. Rev. A **75**(1), 011801 (2007)
28. S.A. Webster, M. Oxborrow, S. Pugla, J. Millo, P. Gill, Phys. Rev. A **77**(3), 033847 (2008)
29. J. Shang, J. Cao, K. Cui, S. Wang, P. Zhang, J. Yuan, S. Chao, H. Shu, X. Huang, Opt. Commun **382**, 410–414 (2017)
30. R. Blümel, C. Kappler, W. Quint, H. Walther, Phys. Rev. A **40**(2), 808 (1989)

31. D. Wineland, H. Dehmelt, Int. J. Mass Spectrom. Ion Phys. **16**(3), 338–342 (1975)
32. J.E. Bernard, A.A. Madej, L. Marmet, B.G. Whitford, K.J. Siemsen, S. Cundy, Phys. Rev. Lett. **82**(16), 3228–3231 (1999)
33. P. Dubé, A.A. Madej, Z. Zhou, J.E. Bernard, Phys. Rev. A **87**(2), 023806 (2013)
34. S. Urabe, M. Watanabe, H. Imajo, K. Hayasaka, U. Tanaka, R. Ohmukai, Appl. Phys. B Lasers Opt. **67** (2), 223–227 (1998).
35. A.A. Madej, J.E. Bernard, P. Dubé, L. Marmet, R.S. Windeler, Phys. Rev. A **70**(1), 012507 (2004)
36. W.M. Itano, J. Res. Natl. Inst. Stand. Technol **105**(6), 829–837 (2000)
37. M. Dolezal, P. Balling, P.B.R. Nisbet-Jones, S.A. King, J.M. Jones, H.A. Klein, P. Gill, T. Lindvall, A.E. Wallin, M. Merimaa, C. Tamm, C. Sanner, N. Huntemann, N. Scharnhorst, I.D. Leroux, P.O. Schmidt, T. Burgermeister, T.E. Mehlstaubler, E. Peik, Metrologia **52** (6), 842–856 (2015).
38. P.B.R. Nisbet-Jones, S.A. King, J.M. Jones, R.M. Godun, C.F.A. Baynham, K. Bongs, M. Dolezal, P. Balling, P. Gill, Appl. Phys. B Lasers Opt. **122**(3), 57 (2016).
39. P. Zhang, J. Cao, H. Shu, J. Yuan, J. Shang, K. Cui, S. Chao, S. Wang, D. Liu, X. Huang, J. Phys. B At. Mol. Opt. Phys. **50**(1), 015002 (2017)
40. W.M. Itano, L.L. Lewis, D.J. Wineland, Phys. Rev. A **25**(2), 1233–1235 (1982)
41. M.S. Safronova, U.I. Safronova, Phys. Rev. A **83**(1), 012503 (2011)
42. P. Dubé, A.A. Madej, M. Tibbo, J.E. Bernard, Phys. Rev. Lett. **112**(17), 173002 (2014)
43. P. Dube, A.A. Madej, A. Shiner, B. Jian, Phys. Rev. A **92**(4), 8 (2015)
44. W. Itano, J. Bergquist, J. Bollinger, J. Gilligan, D. Heinzen, F. Moore, M. Raizen, D. Wineland, Phys. Rev. A **47**(5), 3554 (1993)
45. A. Al-Masoudi, S. Dorscher, S. Hafner, U. Sterr, C. Lisdat, Phys. Rev. A **92**(6), 7 (2015)
46. M. Takamoto, T. Takano, H. Katori, Nat Photon **5**(5), 288–292 (2011).
47. T.L. Nicholson, M.J. Martin, J.R. Williams, B.J. Bloom, M. Bishof, M.D. Swallows, S.L. Campbell, J. Ye, Phys. Rev. Lett. **109**(23), 230801 (2012)